Energetic Neutral Atoms (ENA) at Mars: Properties of the hydrogen atoms produced upstream of the martian bow shock and implications for ENA sounding technique around non-magnetized planets

E. Kallio [a,*], S. Barabash [b], K. Brinkfeldt [b], H. Gunell [b], M. Holmström [b], Y. Futaana [b], W. Schmidt [a], T. Säles [a], H. Koskinen [a,q], P. Riihelä [a], R. Lundin [b], H. Andersson [b], M. Yamauchi [b], A. Grigoriev [b], J.D. Winningham [c], R.A. Frahm [c], J.R. Sharber [c], J.R. Scherrer [c], A.J. Coates [d], D.R. Linder [d], D.O. Kataria [d], J. Kozyra [e], J.G. Luhmann [f], E. Roelof [g], D. Williams [g], S. Livi [f], P. C:son Brandt [g], C.C. Curtis [h], K.C. Hsieh [h], B.R. Sandel [h], M. Grande [i], M. Carter [i], J.-A. Sauvaud [j], A. Fedorov [j], J.-J. Thocaven [j], S. McKenna-Lawler [k], S. Orsini [l], R. Cerulli-Irelli [l], M. Maggi [l], P. Wurz [m], P. Bochsler [m], N. Krupp [n], J. Woch [n], M. Fränz [n], K. Asamura [o], C. Dierker [p]

[a] *Finnish Meteorological Institute, Box 503, FIN-00101 Helsinki, Finland*
[b] *Swedish Institute of Space Physics, Box 812, S-98 128 Kiruna, Sweden*
[c] *Southwest Research Institute, San Antonio, TX 7228-0510, USA*
[d] *Mullard Space Science Laboratory, University College London, Surrey RH5 6NT, UK*
[e] *Space Physics Research Laboratory, University of Michigan, Ann Arbor, MI 48109-2143, USA*
[f] *Space Science Laboratory, University of California in Berkeley, Berkeley, CA 94720-7450, USA*
[g] *Applied Physics Laboratory, Johns Hopkins University, Laurel, MD 20723-6099, USA*
[h] *University of Arizona, Tucson, AZ 85721, USA*
[i] *Rutherford Appleton Laboratory, Chilton, Didcot, Oxfordshire OX11 0QX, UK*
[j] *Centre d'Etude Spatiale des Rayonnements, BP-4346, F-31028 Toulouse, France*
[k] *Space Technology Ltd., National University of Ireland, Maynooth, Co. Kildare, Ireland*
[l] *Istituto di Fisica dello Spazio Interplanetari, I-00133 Rome, Italy*
[m] *Physikalisches Institut, University of Bern, CH-3012 Bern, Switzerland*
[n] *Max-Planck-Institut für Aeronomie, D-37191 Katlenburg-Lindau, Germany*
[o] *Institute of Space and Astronautical Science, 3-1-1 Yoshinodai, Sagamichara, Japan*
[p] *Technical University of Braunschweig, Hans-Sommer-Strasse 66, D-38106 Braunschweig, Germany*
[q] *Department of Physical Sciences, University of Helsinki, P.O. Box 64, FIN-00014 Helsinki, Finland*

Abstract

We have studied the interaction of fast solar wind hydrogen atoms with the martian atmosphere by a three-dimensional Monte Carlo simulation. These energetic neutral hydrogen atoms, H-ENAs, are formed upstream of the martian bow shock. Both H-ENAs scattered and non-scattered from the martian atmosphere/exosphere were studied. The colliding H-ENAs were found to scatter both to the dayside and nightside. On the dayside they contribute to the so-called H-ENA albedo. On the nightside the heated and scattered hydrogen atoms were found also in the martian wake. The density, the energy distribution function and the direction of the velocity of H-ENAs on the nightside are presented. The present study describes a novel "ENA sounding" technique in which energetic neutral atoms are used to derive information of the properties of planetary exosphere and atmosphere in a similar manner as the solar wind photons are used to derive atmospheric densities by measuring the scattered UV light. A detailed study of the direction and energy of the scattered and non-scattered H-ENAs suggest that the ENA sounding is a method to study

* Corresponding author. Fax: +358 9 1929 4603.
E-mail address: esa.kallio@fmi.fi (E. Kallio).

the interaction between the planetary atmosphere and the solar wind and to monitor the density, and likely also the magnetization, of the planetary upper atmosphere. Already present-day ENA instrument should be capable to detect the analyzed particle fluxes.

1. Introduction

An energetic neutral atom, ENA, is formed in a charge exchange process where an energetic ion picks up an electron from a neutral particle. The process is common practically everywhere where ions and neutral atoms exist simultaneously. Mars is in this respect an interesting object because it has no notable global intrinsic magnetic field to shield its exosphere and atmosphere from the flow of the solar wind protons, and, consequently, an extensive production of energetic hydrogen atoms, H-ENAs, takes place.

At Mars, as well as at Venus, solar wind protons are turned into energetic hydrogen atoms in several different plasma regions: (1) in the solar wind upstream of the bow shock, (2) in the magnetosheath downstream of the bow shock, and (3) in the region between the magnetosheath and the surface of the planet. These three populations could be referred to as solar wind (H-ENA$_{sw}$), magnetosheath and induced magnetosphere H-ENAs, respectively, illustrating the site where they were generated. Some of the H-ENAs hit the martian atmospheric/exospheric neutrals resulting in atmospheric effects and the so called H-ENA albedo, that is, energetic hydrogen atoms scattered away from the planet (Kallio and Barabash, 2000, 2001). The H-ENAs which do not collide with neutrals retain the velocity that they obtained when they were generated. These two H-ENA populations form scattered and non-scattered H-ENAs depending on whether or not they have collided with neutral particles after they were generated.

The absolute production rate of H-ENAs at different plasma regions near Mars depends on the martian global plasma environment and the density of the martian atmosphere/exosphere, that is, the overall Mars–solar wind interaction. The properties of non-scattered H-ENA populations near Mars have been studied both by a particle model (Kallio et al., 1997) and by an analytical line-of-sight (LOS) model (Holmström et al., 2002; Gunell et al., 2005). The atmospheric effects of scattered solar wind H-ENAs have been studied by a three-dimensional Monte Carlo (3-D MC) model (Kallio and Barabash, 2000, 2001). Scattered H-ENAs form an important ENA population at Mars because their particle flux is substantial, up to several per cent of the flux of the undisturbed solar wind protons due to the small distance of the bow shock and the large exospheric scale heights (see, e.g., Kallio et al., 1997). A notable fraction of initial solar wind protons are therefore transformed into fast energetic hydrogen atoms already before the solar wind meets the bow shock of the planet.

The purpose of this paper is to study the properties of fast hydrogen atoms near Mars that are formed in the undisturbed solar wind. While a previous study (Kallio and Barabash, 2000, 2001) focused on analysis of various atmospheric effects, in this paper we study the properties of the scattered solar wind H-ENAs near Mars by a 3-D MC model. A special emphasis is placed on the study of H-ENAs over 100 eV because they are measured at Mars by two ENA detectors on the ASPERA-3/Mars Express instrument: Neutral Particle Imager, NPI, and Neutral Particle Detector, NPD (see Brinkfeldt et al., 2006; Futaana et al., 2006; Gunell et al., 2006, for the details of the NPI and NPD observations). The analysis of the properties of the scattered H-ENAs formed in the magnetosphere or in the induced magnetosphere is not included in this paper because their properties depend on the overall Mars–solar wind interaction and the analysis would require a 3-D self-consistent plasma model.

The properties of the scattered solar wind H-ENA atoms depend both on the properties of the solar wind protons and on the properties of the exosphere/atmosphere upon which ions are impacting. The problem analyzed here is of a wider general interest because, as illustrated later in this paper, measuring the properties of these ENAs provides information about planetary atmosphere and the properties of the solar wind plasma influencing the atmosphere.

The paper is organized as follows. First, we briefly describe the 3-D MC model. Second, we study the properties of the scattered solar wind H-ENAs at Mars. Then macroscopic parameters for three energy ranges and the direction of the scattered H atoms at several vantage points on the nightside are examined. We also calculate the differential directional fluxes for a virtual ENA instrument with the field-of-view similar to NPI on Mars Express, and analyze how non-scattered solar wind H-ENAs fill the martian tail. Then we compare the flux of scattered H-ENAs with the flux of the non-scattered H-ENAs produced upstream and downstream of the bow shock and calculate at what altitudes the particles are scattered. Finally, the possibilities of the new ENA sounding technique for a planetary research are discussed.

2. Formulation of the problem and the description of the model

The most important source mechanisms to generate H-ENAs near Mars are collisions of fast solar wind protons (H_f^+) with the atmospheric and exospheric hydrogen (H_{cold}) and oxygen (O_{cold}) atoms:

$$H_f^+ + H_{cold} \rightarrow H_f + H_{cold}^+,$$

$$H_f^+ + O_{cold} \rightarrow H_f + O_{cold}^+.$$
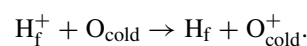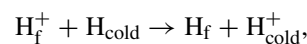
In those charge exchange processes a fast ($E > 1$ eV) solar wind proton takes an electron from a neutral atom forming a new cold hydrogen or oxygen ion. The fast proton loses only a small part of its initial energy. Therefore, the newly born fast
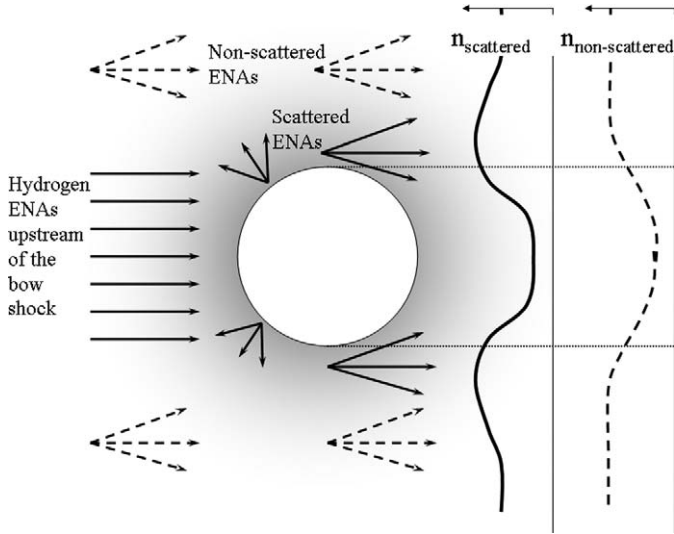
Fig. 1. Illustration of energetic neutral hydrogen atoms near Mars that are formed upstream of the martian bow shock, H-ENA$_{sw}$s. The solid arrows depict the velocity vector of H-ENAs that collide with martian atmospheric neutrals (scattered H-ENA$_{sw}$s). A part of these scattered ENAs is thermalized in the atmosphere and another part is scattered from the martian atmosphere. The latter forms a part of the ENA albedo. The dashed arrows illustrate the velocity of the H-ENAs formed also upstream of the bow shock, but moving so far above the martian exopause that their orbits are typically almost straight lines. The solid (dashed) line illustrates the density of the scattered (non-scattered) H-ENA$_{sw}$ population on the nightside.

H-ENA carries almost undisturbed information about the momentum of the initial fast proton.

Fig. 1 illustrates the two solar wind H-ENA populations analyzed in this paper: The scattered solar wind H-ENAs and the non-scattered solar wind H-ENAs. The scattered H-ENA$_{sw}$s are formed upstream of the bow shock and they move close to or below the exopause where collisions become important. That population was modeled by launching $100\,000$ cold ($T = 0$ eV) H atoms toward Mars with the solar wind velocity of $\mathbf{U}_{sw} = [-400, 0, 0]$ km s^{-1}. The particles were launched on the dayside from the hemisphere at $h = 650$ km above the surface, i.e. at $r = 1.19 R_M$ ($R_M =$ the radius of Mars $= 3393$ km) well above the exopause. The path of the particles was calculated by the same 3-D MC model that was developed to study the effects of the precipitating solar wind protons to the martian atmosphere (Kallio and Janhunen, 2001). The 3-D MC model contains 30 collision processes between two projectile types (H and H$^+$) and three types of targets (CO$_2$, N$_2$, O): Six elastic and 24 inelastic (ionization of the target and H atom, charge exchange, electron stripping, Lyman and Balmer alpha emissions).

The properties of the H-ENAs derived from the 3-D MC model are axially symmetric with respect to the direction of the solar wind flow because the model does not contain the effects of the Lorentz force. In reality, a non-zero Lorentz force introduces some asymmetry to the properties of H-ENAs near Mars because the initial fast hydrogen atoms (H$_f$) can transform into protons (H$^+$) also by electron stripping:

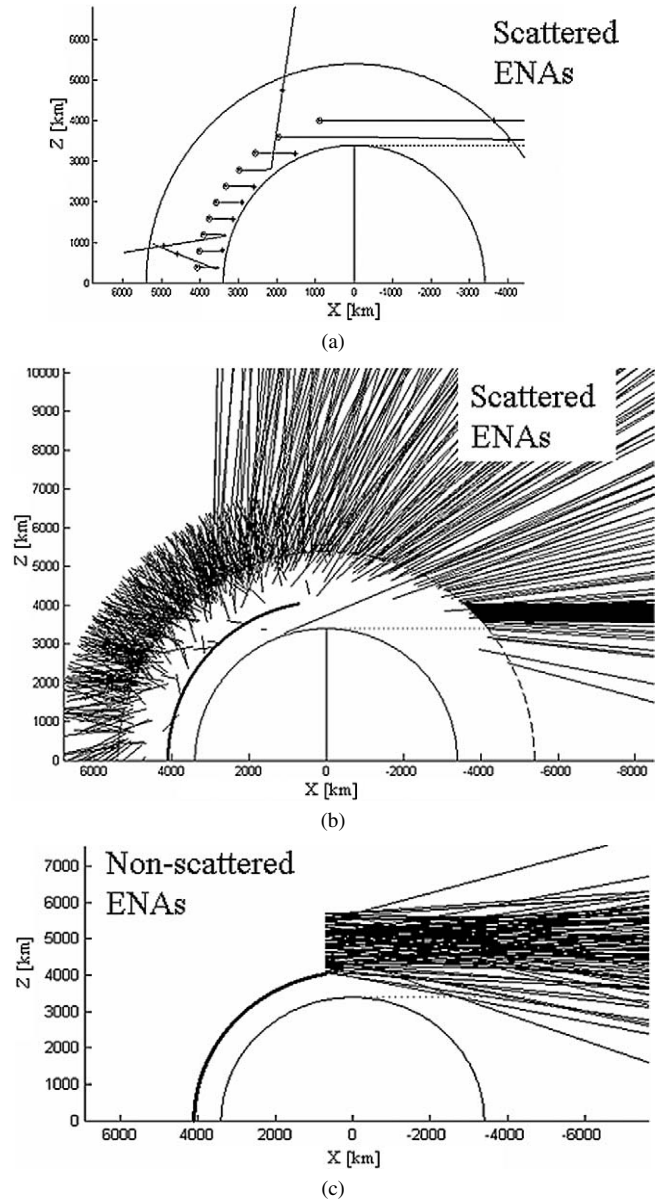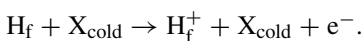$$H_f + X_{cold} \rightarrow H_f^+ + X_{cold} + e^-.$$

Fig. 2. (a) An example of trajectories of ten hydrogen atoms near Mars. Cold ($T_{sw} = 0$ eV) hydrogen atoms were launched at 650 km above the martian surface and their trajectories were calculated by the 3-D Monte Carlo model. The positions and the velocities of the ENAs were recorded when they hit a spherical shell of 2000 km above Mars (the solid circle). (b) 3-D trajectories of 2000 H-ENAs launched at the spherical shell. The short (long) lines present the orbits of 1000 H-ENAs which have the velocity $v_x > 0$ ($v_x < 0$). All trajectories are plotted starting at $h = 2000$ km. (c) An example of 3-D trajectories of the non-scattered hot ($T_{sw} = 20$ eV) hydrogen ENAs. These particles were launched at $x = 0.2 R_M$.

Here X_{cold} is a neutral atom or molecule and e^- is an electron. Also, a particle that is scattered from Mars as a hydrogen atom may have spent part of its life time in the martian atmosphere as a proton under the influence of a non-zero Lorentz force. Possible asymmetries resulting from the direction of the interplanetary magnetic field, IMF, and the observed martian magnetic anomalies (Acuña et al., 1998) are not taken into account in this paper. The atmosphere and exosphere are also assumed to be stationary and spherically symmetric and therefore, spatial and temporal variations are disregarded.
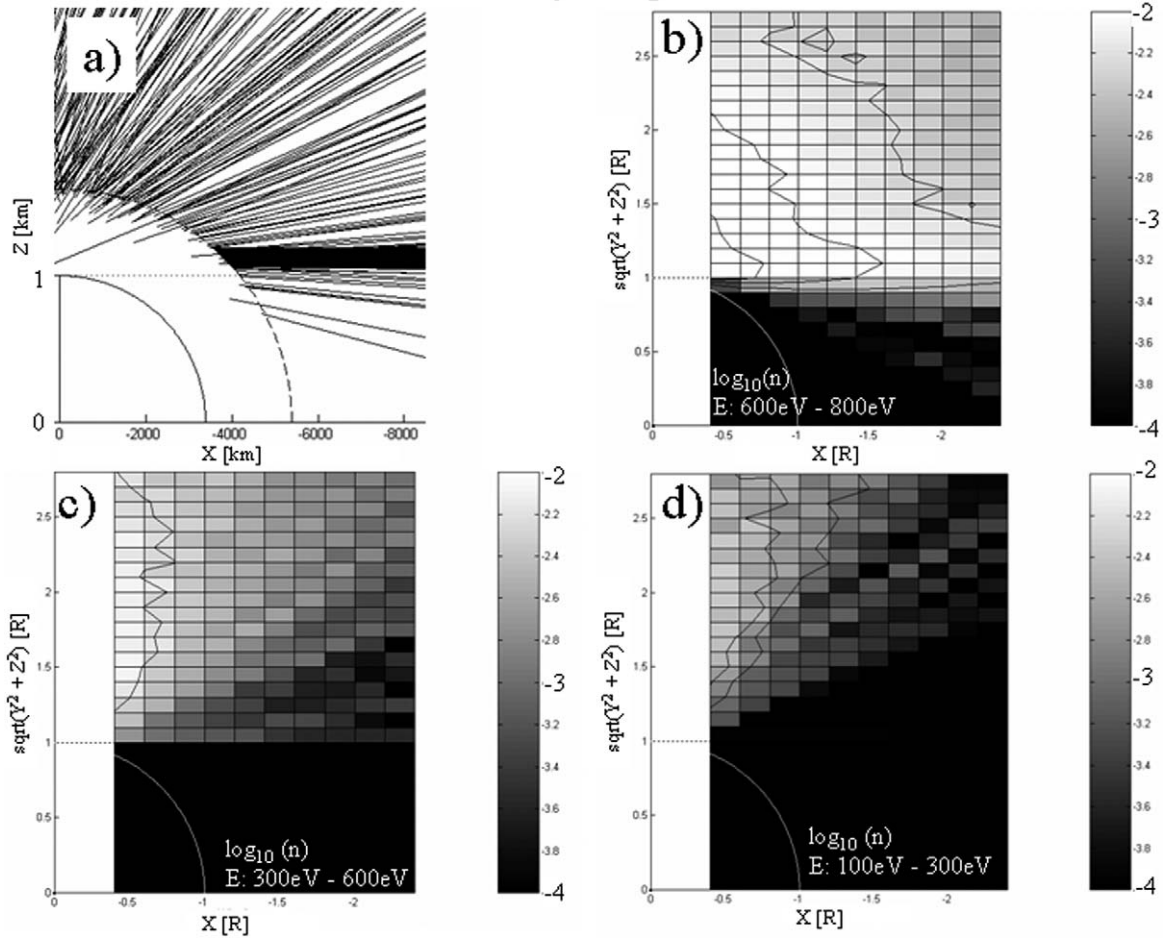
Scattered SW hydrogen ENAs

Fig. 3. The properties of solar wind H-ENAs near Mars based on a 3-D MC model. (a) An example of trajectories of the scattered solar wind H-ENAs on the nightside. (b, c, d) The density of the solar wind H-ENAs that have collided with martian neutrals normalized by the density of the undisturbed hydrogen ENAs: (b) $600\,eV < E < 800\,eV$, (c) $300\,eV < E < 600\,eV$, and (d) $100\,eV < E < 300\,eV$. The contours in (b) show the normalized densities 0.02, 0.01, and 0.005, contours in (c) the value 0.005, and contours in (d) 0.002 and 0.001. The energy of the upstream H-ENAs was $\sim$850 eV.

In the 3-D MC model the trajectory of a particle was followed until its energy became less than 100 eV or its altitude from the surface of Mars became larger than 2000 km. The value of the energy threshold was chosen to correspond to the minimum energy that can be observed by a modern ENA instrument, especially, such as NPI/ASPERA-3 on Mars Express. Fig. 2a illustrates the trajectories of ten fast hydrogen atoms near Mars based on the 3-D MC simulation. Five of the ten particles remain in the martian atmosphere their energies becoming smaller than the 100 eV energy thresholds. Three H-ENAs are scattered back resulting in an ENA albedo.

Note that in Fig. 2a the trajectories of two particles launched at $x < 2000$ km are almost straight lines. They illustrate the fact that when the solar zenith angle (SZA) is close to 90° the number of collisions becomes small. For example the H-ENA in Fig. 2a launched at $x \sim 1000$ km has not collided with a single atmospheric neutral. Therefore, in this paper the second ENA population was modeled by launching H-ENAs from the plane $x = 0.2 R_M$ with $1.19 R_M < \rho = \sqrt{y^2 + z^2} < 1.68 R_M$ (cf. Fig. 2c). This source is far above the martian exobase and, consequently, these ENAs seldom collide with martian atmospheric

neutrals. These ENAs are assumed to be fully non-scattered in order to reduce the computation time. This assumption is not expected to result in notable errors because the probability of H-ENAs launched from $h = 650$ km at SZA $\sim 90°$ to collide with neutrals is very small (see also Figs. 2a and 2b). The temperature of the hydrogen atoms was chosen to be 20 eV. Fig. 2c gives an example of the paths of about one hundred non-scattered ENAs on the nightside. Note that in Fig. 2 the particles were launched on the XZ plane but the trajectories are three-dimensional making it difficult to visualize their motion near the planet. Nevertheless, some of these particles seem to fill the martian wake and this will be shown later in Section 4.

3. Scattered solar wind H-ENAs

Here we study the properties of H-ENAs on the martian nightside region. Fig. 3a shows the details of the trajectories of the solar wind ENAs in the analyzed spatial region illustrating how the collisions heat the original cold ENA beam, while Figs. 3b–3d depict the normalized density of H-ENA$_{sw}$s in three energy ranges below the energy of H-ENAs. Scattered
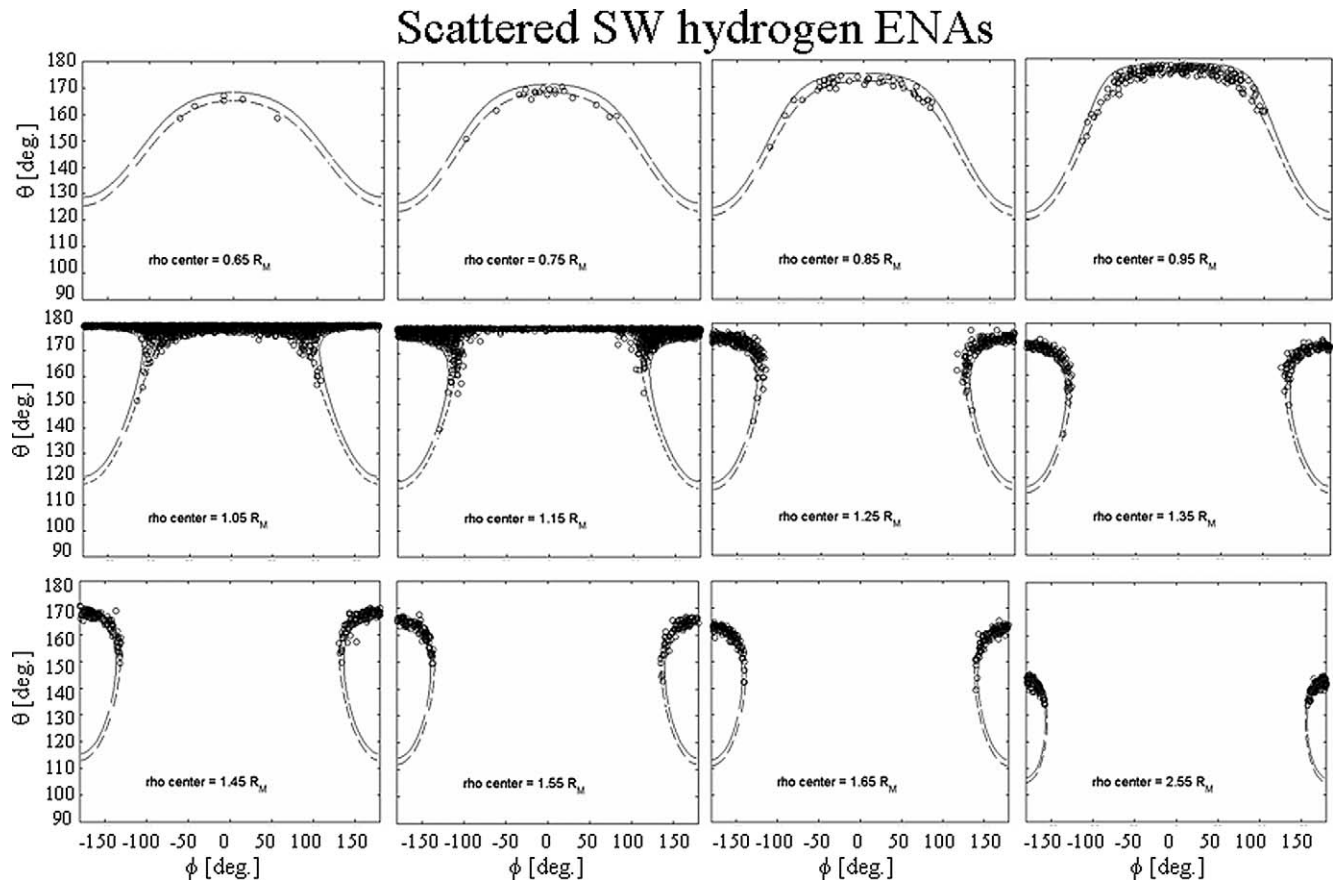
Scattered SW hydrogen ENAs

Fig. 4. The direction of scattered solar wind ENAs collected by virtual ENA detectors at $x = -1.8 R_M$ centered at twelve ρ_{center} distances from $0.65 R_M$ to $2.65 R_M$. Collected hydrogen ENAs are shown with circles by the solid and dashed lines show the limb of Mars and limb of a sphere at $h = 300$ km, respectively. Note the limb brightening at $h < 300$ km. See text for details.

H-ENAs form the most interesting ENA population analyzed in this work because they manifest the interaction between the solar wind hydrogen ENA beam and martian neutrals and thus they carry information about the neutrals with which they have collided.

The high energy interval 600 eV $< E < 800$ eV includes only hydrogen ENAs that have had collisions with martian neutrals because the energy of the collected H-ENAs is below their initial energy of ~ 850 eV (~ 400 km s^{-1}) (Fig. 3b). The maximum normalized density value in Fig. 3b is much less than one because it contains only H-ENAs that have interacted with Mars. The maximum density, a few per cent of the initial density of H-ENAs, can be found near the optical shadow at $\rho \sim 1.1 R_M$. Note also that the density within the optical shadow of Mars is non-zero resulting from the scattering and the heating of the originally cold H-ENA$_{sw}$s from high SZA values.

The relative densities in the medium energy range 300 eV $< E < 600$ eV (Fig. 3c) and in the low energy range 100 eV $< E < 300$ eV (Fig. 3d) correspond to the H-ENAs that have collided many times with martian neutrals. The ENAs with $E < 600$ eV form an "ENA halo" around Mars. That does not extend to the optical shadow of Mars. Comparison of Figs. 3b and 3c also shows how the energy distribution changes on the nightside when moving away from the x-axis: The optical shadow is filled with 600 eV $< E < 800$ eV ENAs. The region just out

of the optical shadow contains also 300 eV $< E < 600$ eV ions while ions in the energy range 100 eV $< E < 300$ eV can be observed further away from the x-axis.

Fig. 4 illustrates the direction of H-ENAs collected at $x = -1.8 R_M$ at twelve ρ values between $0.6 R_M < \rho < 2.6 R_M$. Every circle corresponds to a hit of an ENA on a d$\rho = 0.1 R_M$ band. For example, the H-ENAs collected at $\rho_{center} = 0.65 R_M$ (Fig. 4, the panel on the upper left corner) corresponds to H-ENAs collected at $0.6 R_M < \rho < 0.7 R_M$. The direction is presented in a polar coordinate system, the polar z-axis pointing against the flow of the solar wind and the polar x-axis pointing radially away from the Mars–Sun axis. The undisturbed cold ($T_{SW} = 0$ eV) solar wind particles will therefore be at $\theta = 180°$ and particles moving radially toward (outward from) the Mars–Sun line will have $\phi = 0°$ ($\phi = \pm 180°$).

It is worth noting that the initial cold H-ENA$_{sw}$ beam would result in ENA hits on $\theta = 180°$ for the vantage points $\rho_{center} > 1 R_M$. In Fig. 4, however, hydrogen ENAs are observed also at $\rho_{center} < 1 R_M$ due to the scattering caused by collisions. Collisions result in spreading of H-ENAs to a finite ϕ range. The ϕ values of the collected ENAs within the optical shadow are scattered around $0°$ indicating that the collected particles are moving into the optical shadow. Far above the optical shadow at $\rho > 1.45 R_M$, ϕ is $\sim \pm 180°$ indicating that the particles move away from Mars. At $\rho_{center} = 1.05 R_M$ and $\rho_{center} = 1.15 R_M$,
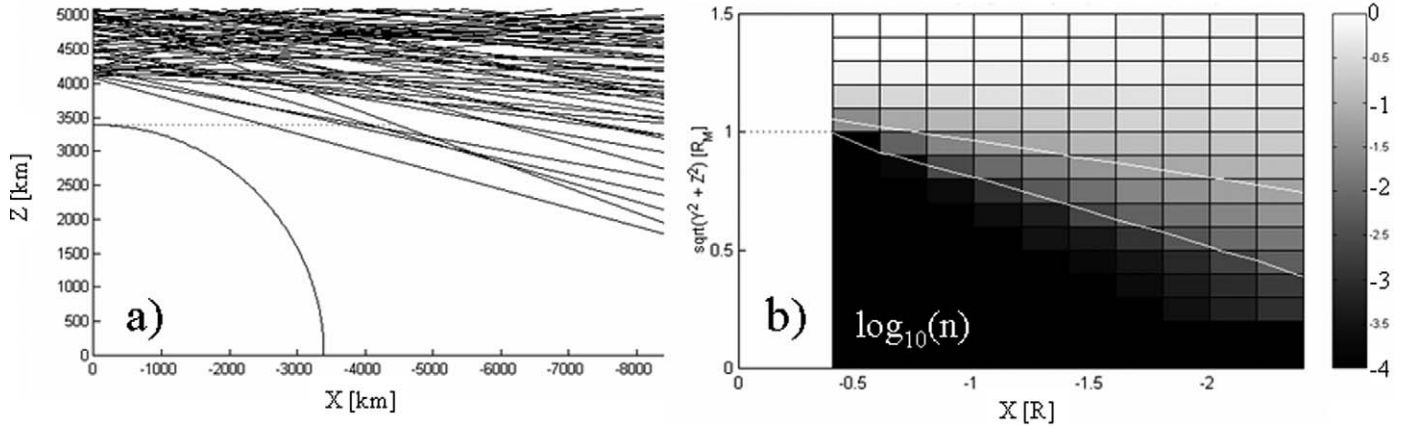
Non-scattered SW hydrogen ENAs

Fig. 5. (a) Trajectories of hot ($T_{sw} = 20$ eV) non-scattered solar wind H-ENAs on the nightside. (b) The corresponding normalized density of H-ENAs in a logarithmic ($\log_{10}$) scale. The two white lines indicate the values 0.1 and 0.01. Note that the filling of the wake with hydrogen atoms resulting from the non-zero initial temperature.

one can identify both frequently collided ENAs ($\theta < 180°$) and seldom or never collided ENAs ($\theta \sim 180°$). The population of the never collided ENAs disappears at $\rho_{center} > 1.25 R_M$ because the hemispherical ENA source on the dayside does not extend beyond $1.19 R_M$. Note also that Fig. 4 suggests that collecting of ENAs only at about $\theta \leqslant 175°$ would filter out the ENAs which have had several collisions with the seldom or never collided ENAs. In practice an ENA instrument contains such a filter because detectors are designed to be protected against the solar UV radiation.

4. Non-scattered solar wind H-ENAs

Our next task is to study the properties of H-ENAs coming from $\rho > 1.19 R_M$ which have not collided with the martian atmosphere/exosphere. Fig. 5a shows in detail the trajectories of these non-scattered solar wind ENAs near the optical shadow on the nightside. Only the orbits at about $z \leqslant 5000$ km and $x > 8000$ km were displayed and analyzed because that region does not include any artificial decrease of the ENA flux outside of the optical shadow caused by the used $1.19 R_M < \rho < 1.68 R_M$ particle source region (cf. Fig. 2c). The relative density of these non-scattered ENAs is shown in Fig. 5b. A notable feature is that these ENAs can be detected in the martian tail because of the thermal spreading of $T_{sw} = 20$ eV hydrogen ENAs.

The direction of H-ENAs collected by virtual ENA detectors at $x = -1.8 R_M$ between $0.3 R_M < \rho < 1.5 R_M$ are given in Fig. 6. There are two basic differences between the direction of the non-scattered H-ENAs given in Fig. 6 and the scattered H-ENAs shown in Fig. 4. First, the non-scattered ENAs form a wide band at about $160° < \theta < 180°$ resulting from the thermal spreading of $T = 20$ eV ENAs. Note that cold $T = 0$ eV ENAs would, on the contrary, result in hits only at $\theta = 180°$ The second difference is that the non-scattered ENAs can be found predominantly outside of the limb of the $h = 300$ km sphere (Fig. 6) while the scattered ENAs are typically seen between the limb of Mars and the limb of the $h = 300$ km sphere

(Fig. 4). The difference results from the fact that the origins of the source of the scattered and non-scattered H-ENAs are different; the scattered ENAs originate closer to Mars than the non-scattered ENAs.

5. ENA sounding

Figs. 1–6 have shown several basic properties of the solar wind H-ENAs on the nightside of Mars. The properties of these H-ENAs depend both of the properties the solar wind plasma and martian atmospheric and exospheric neutrals. In this section we focus on how H-ENAs can be used to study the properties of the solar wind, the martian atmosphere and the Mars–solar wind interaction in general.

We have so far shown that there is no sharp "ENA shadow" behind the planet. The ENA shadow resembles the optical shadow of Mars which is not sharp due to the scattering of light in the atmosphere. Both scattered and non-scattered ENAs were found to protrude into the wake where the velocity distribution function and the macroscopic plasma parameters can be monitored by an ENA instrument. In the eclipse a natural shield for an ENA instrument against the most intense UV radiation is formed.

Comparison of the velocity directions of the scattered H-ENAs (Fig. 4) with the non-scattered H-ENAs (Fig. 6) in the martian tail suggests that an ENA instrument with a good angular resolution can be used to distinguish these two populations from each other. Such an ENA instrument could monitor simultaneously both the upstream plasma parameters and the properties of the martian atmospheric neutrals that have scattered ENAs. The required field of view (FOV) that enables this distinction between the scattered and non-scattered populations depends on the vantage point and thus on the orbit of the spacecraft. For example, the vantage points used in Figs. 4 and 6 would require a FOV of about $5° \times 5°$ at maximum. Such a FOV would also be small enough to resolve the temperature of the non-scattered ENAs by measuring the (thermal) spread
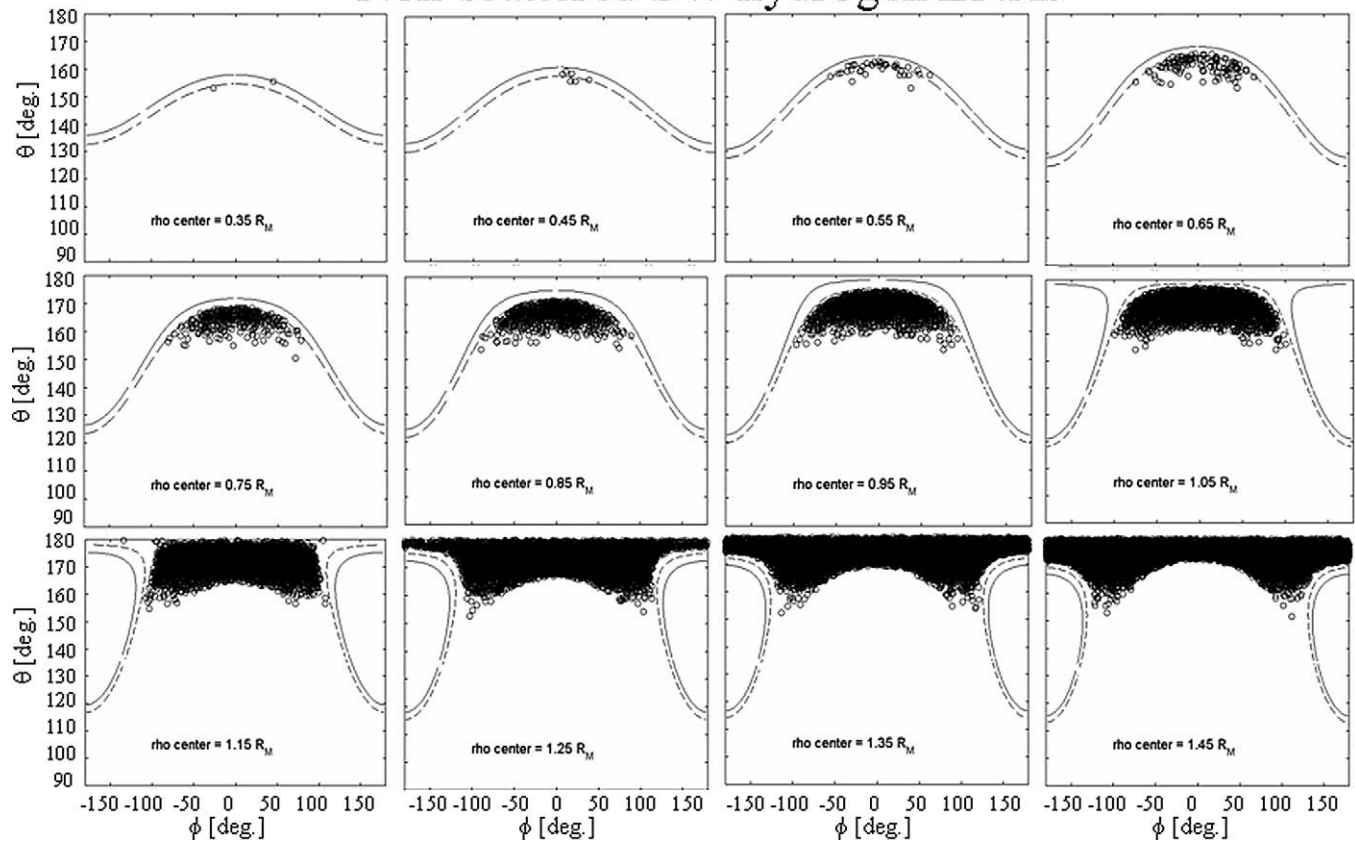
Non-scattered SW hydrogen ENAs

Fig. 6. The direction of the non-scattered H-ENAs collected by virtual ENA detectors at $x = -1.8R_M$ centered at twelve ρ_{center} distances from $0.35R_M$ to $1.45R_M$. The collected hydrogen ENAs are shown by circles while the solid and dashed lines show the limb of Mars and the limb of a sphere at $h = 300$ km, respectively. See text for details.

of the non-scattered ENAs (see Fig. 6). For comparison, the NPI/ASPERA-3 instrument has a FOV of about $4° \times 11.25°$ and NPD/ASPERA-3 about $5° \times 30°$.

Furthermore, Fig. 3 showed that the energy distribution of the scattered H-ENAs depends on the distance from the x-axis, that is, from the Mars–Sun line. Consequently, an ENA instrument with energy resolution is expected to provide new information about the properties of the martian atmosphere by monitoring the energy distribution function. An ENA instrument with only three energy intervals would be enough to capture some basic trends of the energy distribution function of H-ENAs (compare Figs. 3b–3d).

It is therefore informative to study in more detail what an imaginary ENA instrument with both spatial and energy resolution would observe on the nightside of Mars. Let us assume that the virtual ENA instrument has a FOV much as NPI/ASPERA-3: 32 detectors (sectors 0–31), each FOV of $5° \times 11.25°$, collecting H-ENAs on the NPI aperture plane (Barabash et al., 2004). Let us then assume that the NPI aperture plane is on the x–ρ-plane of the 3-D MC model, that is, the vector perpendicular to the NPI aperture plane is perpendicular to the model x-axis. Finally, let the direction between the sectors 0 and 31 point away from the x-axis and the direction between the sectors 23 and 24 point against the direction of the solar wind (see the inset in Fig. 7 in the upper right corner). The

simulated flux contains H-ENAs above the energy threshold of 100 eV used in the MC simulation and this energy is also the minimum energy in NPI/ASPERA-3 instrument.

The bulk velocity of H-ENAs is determined by the MC model ($U_{sw} = 400$ km s^{-1}). However, in order to obtain the absolute differential directional H-ENA flux, j [cm^{-2} s^{-1} str^{-1}], we have to specify the density of H-ENAs at various places of the martian bow shock, $n_{swENA}(\mathbf{r})$. The value of n_{swENA} depends on the density of the martian hydrogen exosphere, on the distance and the shape of the bow shock, and on the density and velocity (charge exchange cross section is energy dependent) of the solar wind. The exospheric density varies with the intensity of the UV radiation and the distance of the bow shock depends on the properties of the solar wind and the IMF. A careful estimate of the n_{swENA} would therefore require a self consistent 3-D Mars–solar wind interaction model for different periods of the solar cycle, which is beyond the scope of this paper. Here we just derive the flux for $n_{swENA}(\mathbf{r}) = 0.125$ cm^{-3}. Such a density could be obtained, for example, if 5% of the solar wind protons with the density of 2.5 cm^{-3} are transformed to H-ENAs upstream of the bow shock. That corresponds to the flux of the solar wind H-ENAs of 5×10^6 cm^{-2} s^{-1} ($= 400 \times 10^5$ cm s^{-1} $\times 0.125$ cm^{-3}). The calculated flux depends linearly on n_{swENA} and the presented flux can therefore be rescaled afterward for a given n_{swENA}.
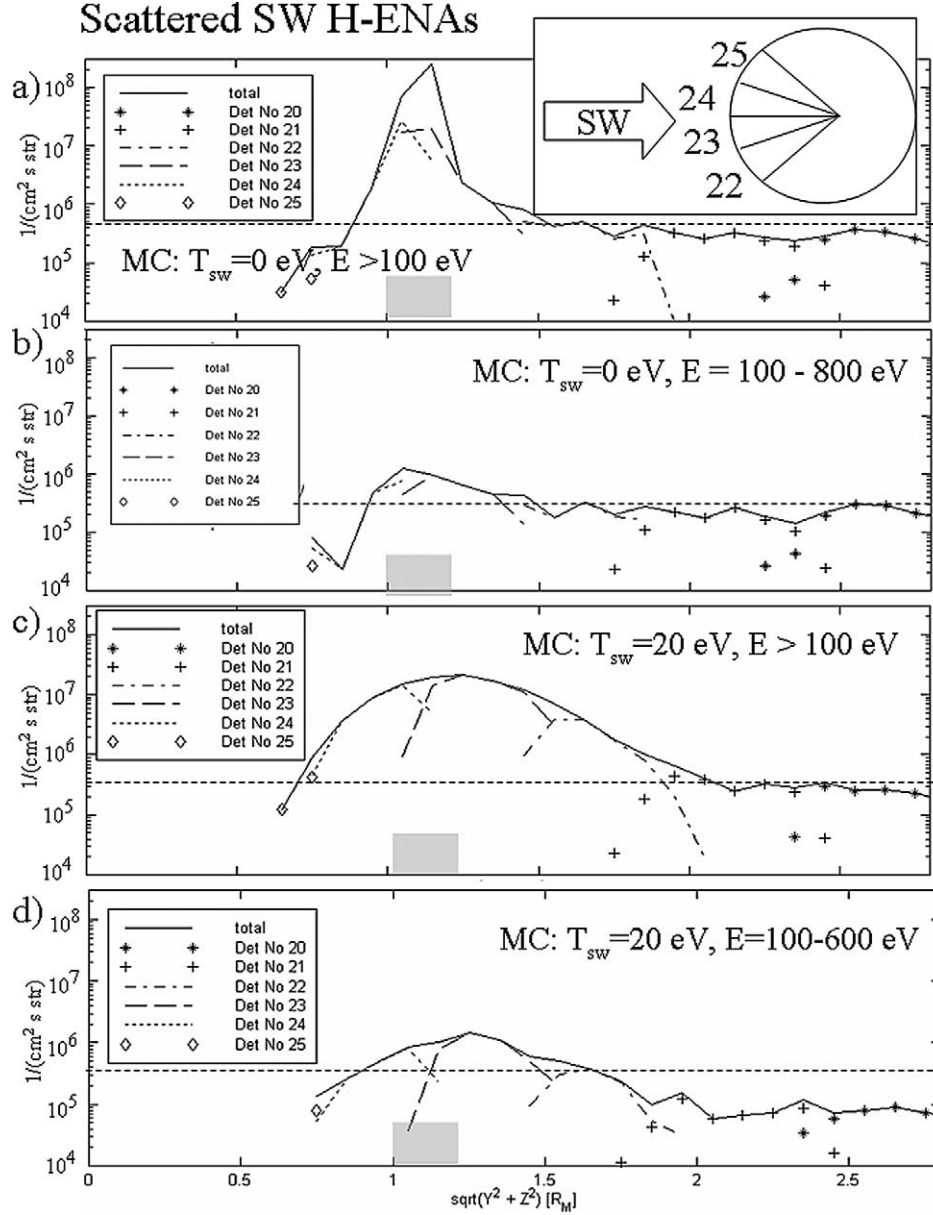
Scattered SW H-ENAs

Fig. 7. The simulated differential directional H-ENA flux j [cm^{-2} s^{-1} str^{-1}] of the scattered H-ENA population measured by a virtual NPI/ASPERA-3 type ENA instrument at $x = -1.8R_M$. The solid lines represent the sum of the fluxes measured by individual NPI sectors. The numbering of the NPI sectors relative to the direction of the solar wind velocity vector is shown in the upper right corner (see text for the details about the virtual ENA detector). The flux is measured in the energy ranges $E > 100$ eV (a) and 100 eV $< E < 800$ eV (b) from the cold ($T_{sw} = 0$ eV) solar wind model and in the energy ranges $E > 100$ eV (c) and 100 eV $< E < 600$ eV (d) from the warm ($T_{sw} = 20$ eV) solar wind model. The horizontal dashed lines show the flux of 3.7×10^5 cm^{-2} s^{-1} str^{-1}. The shaded bar at $1.0R_M < \rho < 1.19R_M$ gives the region of the hemispherical source at $h = 650$ km that is visible when viewed in the tail toward Mars. The vertical log$_{10}$ scale is from 1×10^4 to 3×10^8 cm^{-2} s^{-1} str^{-1}. The values are based on the flux of the solar wind H-ENAs of 5×10^6 cm^{-2} s^{-1} str^{-1}.

We study separately the scattered H-ENAs and the non-scattered H-ENAs. We start with the former population presented in Section 2. The obtained differential directional H-ENA fluxes at $x = -1.8R_M$ for two solar wind temperatures are given in Fig. 7. The values are derived at $x = -1.8R_M$ at the same ρ_{center} and $d\rho = 0.1R_M$ as used in Figs. 4 and 6. The flux is derived for two energy ranges in order to distinguish the H-ENAs launched from the $h = 650$ km hemisphere which have collided with neutrals from the H-ENAs from those which have not. In the MC simulation the energy associated with the bulk velocity of the solar wind protons and, conse-

quently, with the bulk velocity of the H-ENAs formed upstream of the bow shock was ~ 850 eV (~ 400 km s^{-1}). In Fig. 7b the energy window of 100–800 eV is used in order to distinguish this initial undisturbed H-ENA population from the H-ENAs that have lost energy in collisions. The difference between Figs. 7a and 7b indicates that the maximum flux at $\rho = 1.15R_M$ (Fig. 7a) comes from the H-ENAs that have not had many collisions. That population corresponds to H-ENAs seen in Fig. 4a at $\theta \sim 180°$. Note that frequently collided H-ENAs have the maximum flux at $\rho \sim 1R_M$ and that they can be found at $\rho < 1R_M$ (Fig. 7b).
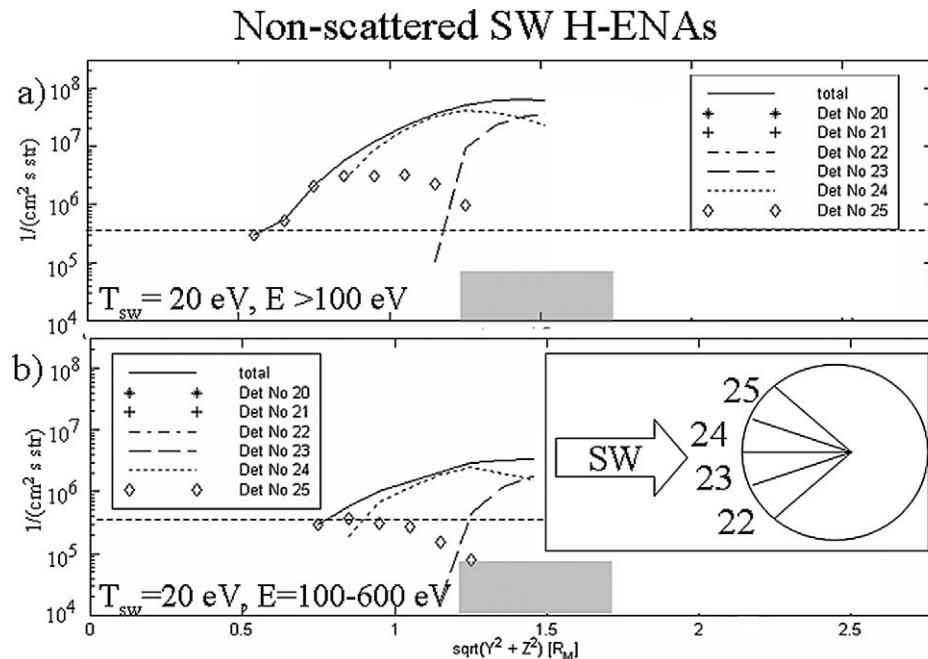
Non-scattered SW H-ENAs

Fig. 8. The simulated differential directional H-ENA flux j [cm^{-2} s^{-1} str^{-1}] of the non-scattered H-ENA population measured by a virtual NPI/ASPERA-3 type ENA instrument at $x = -1.8R_M$. The shaded bar at $1.19R_M < \rho < 1.68R_M$ gives the region of the plane source at $x = 0.2R_M$. The vertical log$_{10}$ scale is from 1×10^4 to 3×10^8 cm^{-2} s^{-1} str^{-1}. The horizontal dashed lines show the flux of 3.7×10^5 cm^{-2} s^{-1} str^{-1}. The temperature of the solar wind is 20 eV. The values are based on the flux of the solar wind H-ENAs of 5×10^6 cm^{-2} s^{-1}.

The hot ($T_{sw} = 20$ eV) solar wind case results in a smoother total $j(\rho)$ curve (Fig. 7c) than in the cold solar wind case (Fig. 7a). Separation of the frequently collided H-ENAs with the non-frequently collided H-ENAs using an energy window is now more difficult than in the cold solar wind case because the initial population contains H-ENAs of various energies; also H-ENAs of $E < 800$ eV. In Fig. 7d the energy window 100 eV $< E < 600$ eV is therefore used to separate the flux associated with the non-collided H-ENAs from the total flux shown in Fig. 7c. It is worth noting that the total flux is often detected by one sector at a time assuming that the used FOV is small enough to resolve the direction of the maximum flux.

Fig. 8 presents the ENA flux associated with the non-scattered H-ENA population analyzed in Section 3. The flux is presented only up to $\rho = 1.45R_M$ in order to avoid a possible artificial decrease of the flux caused by spatially limited H-ENA source applied in this paper (see Fig. 2c). A comparison of the fluxes of the non-scattered and scattered H-ENAs (Figs. 7a and 7b) collected at the same energy ranges (Figs. 7c and 7d) suggests that the non-scattered population dominates the total flux at $\rho < 1.5R_M$. The properties of H-ENAs measured in this ρ range refer therefore mainly to the properties of the solar wind. On the other hand, the relative fluxes measured by sectors 20–25 are not identical. This is consistent with Figs. 4 and 6 which illustrated that the collected scattered H-ENA and the non-scattered H-ENAs originate from different directions. Figs. 7 and 8 suggest that the FOV of the hypothetical ENA instrument is not accurate enough to tell these two populations apart. As pointed out above, an FOV of about $5° \times 5°$ would be required to distinguish the populations.

The final observation about the flux concerns the applicability of a real ENA instrument to observe the simulated fluxes. The NPI/APERA-3 ENA instrument has a geometrical factor per sector of about 2.7×10^{-3} cm^2 str and the efficiency of the NPI sector at $E \sim 1$ keV of about 10^{-3}. The NPI can therefore observe the flux if it is above the NPI minimum flux of $\sim 3.7 \times 10^5$ cm^{-2} str^{-1} s^{-1}. A comparison of the fluxes shown in Figs. 7 and 8 with the NPI minimum flux suggests that an instrument similar to the current NPI/ASPERA-3 will be able to measure the H-ENAs analyzed in this paper if $U_{sw} = 400$ km s^{-1} and $n_{swENA} = 0.125$ cm^{-3}. A more sophisticated ENA instrument would therefore be able to observe solar wind H-ENAs at Mars, even if n_{swENA} would be smaller than that used in this paper.

6. The solar wind vs the magnetosheath and the magnetospheric H-ENAs

The solar wind H-ENAs represent only one H-ENA population near Mars because H-ENAs are formed also in the magnetosheath and in the "magnetosphere." The properties of H-ENAs formed downstream of the bow shock depend on the properties of protons and consequently on the overall Mars–solar wind interaction. Thus, a comprehensive modeling of the generation and the properties of these H-ENAs requires a self-consistent fine resolution 3-D Mars–solar wind interaction model that takes into account kinetic effects and contains martian magnetic anomalies. One could use, for example, a quasi-neutral hybrid (QNH) model which models ions as particles and electrons as a massless charge neutralizing fluid (see Kallio et al., 2006). However, the spatial resolution of 3-D QNH mod-
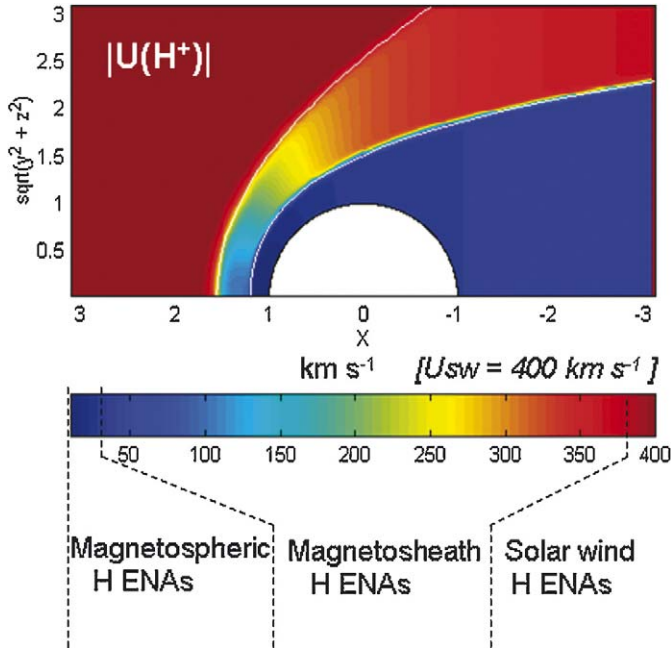
Fig. 9. The bulk velocity of protons at Mars based in an empirical plasma model. In the model the bulk velocity decreases first at the bow shock and thereafter at the magnetopause. Note that the color that shows the value of the bulk velocity color codes also three different H-ENA sources: The solar wind (dark red), the magnetosphere (bark blue), and the magnetosheath (light blue, green, yellow, and light red).

els is not yet good enough to resolve a few kilometer size spatial scales in the martian ionosphere and to include a self-consistently derived ionosphere.

In this section we make a first-order estimation of the relative importance of the H-ENAs formed at three source regions (solar wind, magnetosheath, magnetosphere) by using a semi-empirical analytical plasma model based on ASPERA/Phobos-2 H^+ measurements and line-of-sight (LoS) integration technique. The analytical cylindrically symmetric plasma model gives the velocity of protons and it can be used to derive an estimate for the proton density and temperature (see Kallio et al., 1997). Fig. 9 shows the total velocity in the analytical plasma model for a nominal shape and distance of the bow shock and the magnetopause. In Fig. 9, the solar wind H-ENAs are produced in the (red color) region where $U \sim U_{sw}$. The non-scattered solar wind H-ENAs provide information about the properties of the solar wind protons. The magnetospheric H-ENAs are formed in a (blue color) low velocity region $U \ll U_{sw}$, while the magnetosheath H-ENAs are formed in the region where the velocity is between these high and low velocity regions. A comparison of the properties of H-ENAs derived from the LoS integration from three plasma models, empirical, MHD, and QNH, has shown that the empirical model produced a martian environment qualitatively similar to the MHD and QNH models (Gunell et al., 2005). This suggests that the empirical model can be used to derive first order approximations for the properties of H-ENAs near Mars.

In this section the empirical plasma model and LoS integration are used to study the relative importance of different H-ENA populations first in the terminator plane (Fig. 10) and in

the nightside (Fig. 11) at a point near the region where the properties of H-ENAs were analyzed in the previous section with a 3-D MC model (Figs. 4, 6–8). Distinction of various H-ENAs based on the total flux or on the velocity distribution function is an important issue when in situ H-ENA measurements are analyzed.

The H-ENA sets used in the previous sections were based on the 3-D MC model and collected on the nightside. Therefore, the flux of H-ENAs at $x = 0$ resulting from the charge exchange reaction $H^+ + H$ at solar maximum conditions shown in Fig. 10b is calculated by LoS integration (see Kallio et al., 1997, for details of the empirical plasma model, neutral profiles and cross sections). The integration is performed up to $3R_M$ from the center of Mars the minimum altitude being 210 km from the surface. No attenuation caused by electron stripping is taken into account and, therefore, the derived H-ENA flux may be considered to provide a top limit of the real H-ENA flux. The maximum flux during solar maximum conditions, $\sim 10^6 \, cm^{-2} \, s^{-1} \, str^{-1}$, is associated with the H-ENAs formed in the magnetosheath on the dayside (Fig. 10b). The average solar wind H-ENA albedo based on a previous 3-D MC model study (Kallio and Barabash, 2001) is about 0.58 and, therefore, Fig. 10b shows the flux of H-ENAs from the martian atmosphere based on the assumption that 58% of the impacting solar wind H-ENAs are scattered back to space. Part of the back-scattered H-ENAs also originate downstream of the bow shock, but the flux of the precipitating solar wind H-ENAs is larger that the flux of the precipitating H-ENAs formed at the downstream side (see Kallio and Barabash, 2001, Fig. 4). In Fig. 10c, the solar wind H-ENA flux was assumed to be 1% of the undisturbed solar wind flux of $1.5 \times 10^8 \, cm^{-2} \, s^{-1}$ ($n_{sw} = 3 \, cm^{-3}$, $U_{sw} = 500 \, km \, s^{-1}$).

The superposition of the H-ENA fluxes shown in Figs. 10b and 10c is shown in Fig. 10d. Fig. 10 suggests that the flux of H-ENAs scattered from the martian atmosphere consists mostly of scattered solar wind H-ENAs and only slightly H-ENAs formed in the $H^+ + H$ process between Mars and the vantage point at $x = 0$, $\sqrt{y^2 + z^2} = 2R_M$. Note that the H-ENAs resulting from the process $H^+ + O$ are not presented in Fig. 10 because the flux associated with the process is very sensitive to the properties of H^+ ions at a few hundred kilometers above the Mars where the properties of H^+ ions are highly unknown.

It is worth noting that H-ENAs near the limb come from the H-ENA "thick" region through which H-ENAs cannot pass without collisions with atmospheric neutrals. As already noted before, most of the precipitating H-ENAs are solar wind H-ENAs and the flux of the back-scattered H-ENAs can exceed the flux of the H-ENAs produced between the vantage point and Mars (cf. Figs. 10b and 10c). Therefore, the flux at the limb from the LoS directions with altitudes from the surface smaller than about 200 km can be anticipated to contain mostly scattered solar wind H-ENAs.

In Fig. 11 the relative importance of the upstream and downstream H-ENA production regions is studied by calculating the H-ENA flux at vantage point on the nightside deep in the tail ($x = -1.8R_M$, $\sqrt{y^2 + z^2} = 1.5R_M$) at solar minimum conditions. As seen earlier in Fig. 4, the scattered H-ENAs form
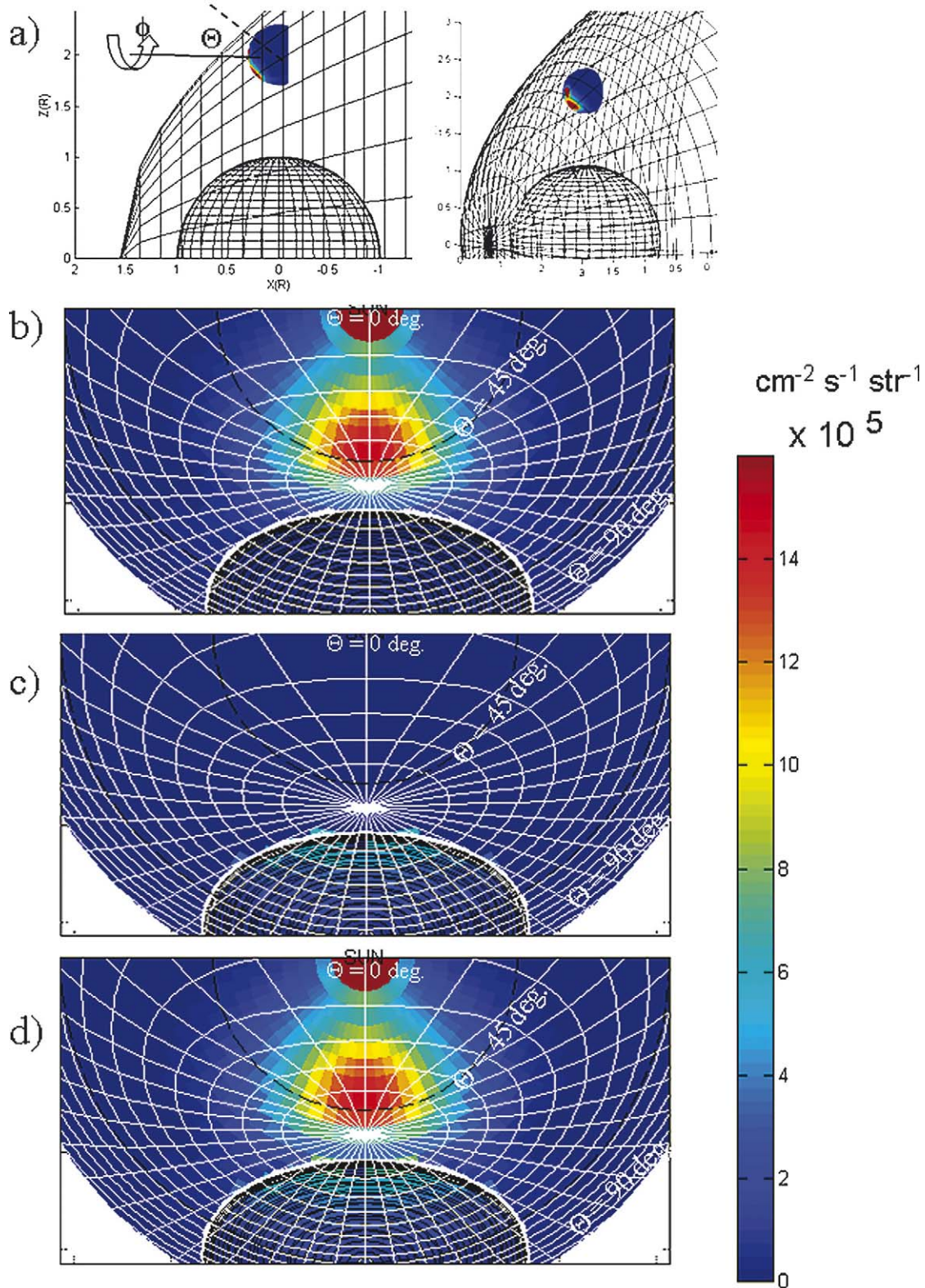
Fig. 10. H-ENA flux at the vantage point $x = 0$, $\sqrt{y^2 + z^2} = 2R_M$. (a) The position of the vantage point is surrounded by a 2π hemisphere. The color on the hemisphere gives the flux of H-ENAs shown in (b). (a, left figure) shows the description the polar theta (θ) and phi (ϕ) angles: θ is the angle between the direction of the LoS line and the line pointing from Mars to Sun, and ϕ is the angle between the LoS line and the line from the vantage point to the x-axis that is perpendicular to the x-axis. The black lines form grids on the surface of the bow shock and Mars. (b) H-ENA flux at the same vantage point associated with the $H^+ + H$ charge exchange process. The white lines are the grid on the surface of the bow shock shown in (a). The highest flux at $\theta = 0°$ are non-scattered solar wind H-ENAs. The flux is calculated for the solar maximum conditions from an empirical plasma model by LoS integration for the solar wind flux of 1.5×10^8 cm^{-2} s^{-1}. (c) The flux of the back-scattered H-ENAs by assuming a constant H-ENA albedo of 0.58. (d) The sum of the H-ENA fluxes shown in (b) and (c). (b), (c), and (d) show the angular view about π str: $0° < \theta < 90°$, $0° < \phi < 90°$, and $270° < \phi < 360°$.
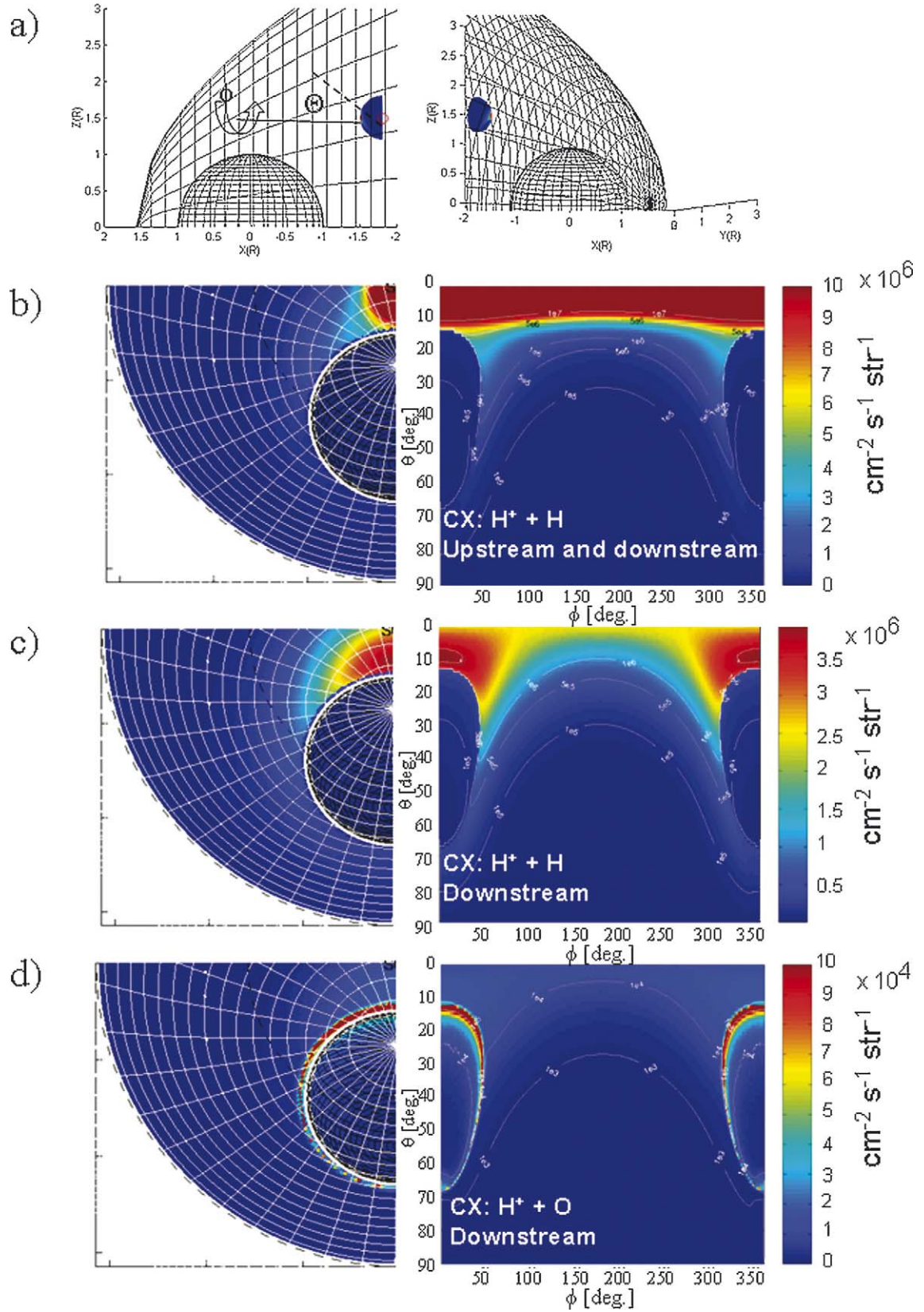
Fig. 11. H-ENA flux at the vantage point $x = -1.8R_{\rm M}$, $\sqrt{y^2 + z^2} = 1.5R_{\rm M}$ at solar minimum. (a) The analyzed position viewed along the y-axis (left) and a 3-D view (right). (b) The total H-ENA flux at the vantage point seen in (a) as a result of $H^+ + H$ processes. (c) The H-ENA flux produced *downstream* of the bow shock from $H^+ + H$ processes. (d) The total H-ENA flux resulting from $H^+ + O$ processes. In (b), (c), and (d) the panels on the left show the flux in an H-ENA "fish-eye" image format in a similar way as in (b), (c), and (d), while the panels on the right show the same flux in a Mercator projection. (b), (c), and (d) show the space angle region of about $\pi/2$ str: $0° < \theta < 90°$, $0° < \phi < 90°$. The solar wind flux was 1.0×10^8 cm^{-2} s^{-1}. See Fig. 10 caption for details of the shown lines.

limb brightening, but Fig. 4 did not provide information about how bright the limb would be compared with the H-ENA flux slightly above the limb.

Fig. 11b, left figure, shows the total H-ENA flux resulting from a $H^+ + H$ process presented in a Mercator projection in a similar way as the 3-D MC H-ENAs were presented in Figs. 4 and 6. Note that (θ, ϕ) angles give the direction of the line-of-sight line so an H-ENA that contributes to the flux at a given LoS direction has the velocity vector opposite to the direction of LoS. The Sun is therefore at LoS direction $\theta = 0°$ in Fig. 11 while the velocity vectors of H-ENAs moving away from the Sun have $\theta = 180°$ in Figs. 4 and 5. The global maximum at $\theta = 0°$ in Fig. 11b is associated to the non-scattered solar wind H-ENAs. Variations of the flux with ϕ result from the shadow of Mars, the shape of the bow shock and the magnetopause, and from the spherically symmetric exosphere H density profile. That is seen in Fig. 11c in which only the contribution of H-ENAs formed downstream of the bow shock is taken into account. The maximum H-ENA flux in Fig. 11c is $\sim 4 \times 10^6$ cm^{-2} s^{-1} str^{-1} and it originates from the magnetosheath between the Sun and the limb of Mars.

Figs. 11b and 11c do not include the contribution of the O corona or the O atmosphere. As noted before in Fig. 10, the estimate of the flux resulting from $H^+ + O$ processes near the surface is highly uncertain because the flux of H^+ near Mars is unknown. Nevertheless, Fig. 11c may give a hint of the H-ENA flux resulting from the $H^+ + O$ process. The H-ENA flux is highest near the limb where the density of O atoms is highest. Note that the highest flux of $\sim 1 \times 10^5$ cm^{-2} s^{-1} str^{-1} from $H^+ + O$ processes is much smaller that the highest flux ($> 1 \times 10^6$ cm^{-2} s^{-1} str^{-1}) associated with $H^+ + H$ processes.

7. H-ENAs and the properties of the upper atmosphere

Previous sections considered the properties of the scattered H-ENAs above the exobase. In this section we address the question what does these H-ENAs imply to the properties of the non-magnetized and magnetized upper atmospheres.

7.1. Non-magnetized upper atmosphere

In this paper the non-magnetized upper atmosphere case was analyzed quantitatively by a 3-D MC model. The altitude where most of the collisions takes place depends on the differential scattering cross sections and, therefore, of the type of collision process. Earlier studies have shown that in the 3-D MC model the maximum ionization production rate, the maximum energy deposition rate and the maximum photoemission rate take place at an altitude of about 120–130 km (Kallio and Barabash, 2001).

Fig. 12, instead, shows a function which is important when the height of the H-ENA emission is considered: The minimum altitude of the back-scattered solar wind H-ENAs, $f_{\text{h-min}}$. The figure illustrates that most of the back-scattered H-ENAs had collisions in the altitude range about 120–140 km (for an example of trajectories in the atmosphere see Kallio and Barabash, 2000, Fig. 2). Practically none of the back-scattered H-ENAs
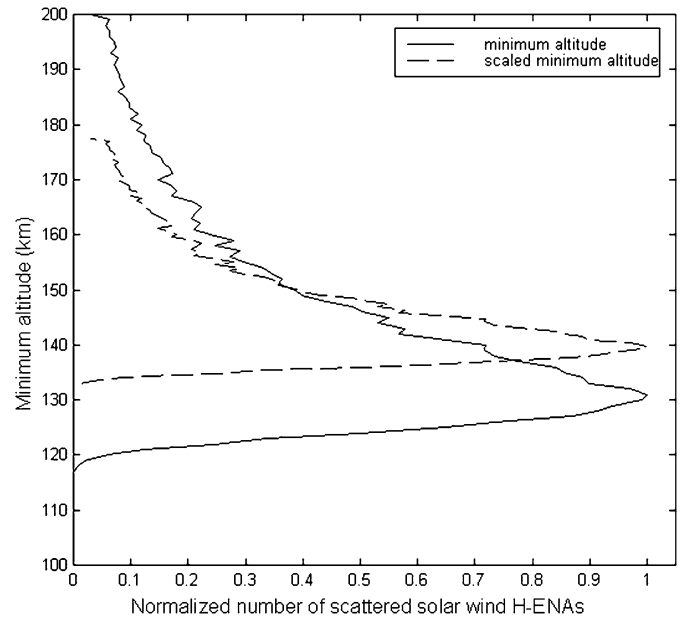

Fig. 12. The minimum altitude distribution function, $f_{\text{h-min}}$, of the back-scattered solar wind H-ENAs from the martian atmosphere based on the 3-D MC model. The solid line shows $f_{\text{h-min}}$ resulting from the atmospheric density profile used in this paper. The dashed line gives an estimation for $F_{\text{h-min}}$ for another atmospheric density profile according to Eqs. (4a) and (4b) (see text for details). The altitude range 100 km < h < 200 km was binned in 1 km height intervals.

have penetrated below about 120 km and most of the H-ENAs have had the minimum altitude around 130 km. Consequently, the properties of the backscattered H-ENAs depend on the properties of the atmosphere at the altitude range about 120–160 km.

It has been shown that the dependence of the atmospheric effects of the precipitating H-ENAs can be described quite well with a continuous slowing down approximation, CSDA (Kallio and Barabash, 2000). In the CSDA model the energy deposition, dE, within the length, dl, depends on the amount of matter through which particles have traversed, that is $dE/dl \sim n$, where n is the density of neutrals. When the atmospheric effects of impacting particles to an atmosphere are considered, the critical parameter is therefore the column density, $N(h)$ [m^{-2}] from infinity to the altitude h.

A notable feature in CSDA is that, as long as the SZA is large enough to consider the scattering process in a plane-parallel geometry, the atmospheric effects depend only on the column density through which particles have moved. Consequently, the altitude profile $F_1 = F_1(h)$ that describes atmospheric effects, for example, ionization, energy deposition, photon emission, or the minimum altitude (Fig. 12), derived for one neutral species atmosphere n_1 can be used to derive the altitude profile $F_2 = F_2(h)$ for another density profile n_2 by mapping the corresponding column densities $N_1 = N_1(h)$ and $N_2 = N_2(h)$ in the following way. Assume, for simplicity, that the density profiles n_1 and n_2 are isothermal atmosphere profiles,

$$n_1 = n_1(h) = n_{01} \exp(-h/H_1), \tag{1}$$

$$n_2 = n_2(h) = n_{02} \exp(-h/H_2). \tag{2}$$

Let us then find the height $h = h_2$ where the column density N_2 is equal to the column density N_1 at height $h = h_1$,

$$N_2(h_2) = N_1(h_1). \tag{3}$$

The solution of Eqs. (1)–(3) is

$$h_1 = Ah_2 + B, \tag{4a}$$

$$A = H_1/H_2, \qquad B = H_1 \ln\big[(H_1 n_{01})/(H_2 n_{02})\big]. \tag{4b}$$

Equations (4) represent a linear coordinate transformation that maps the known profile F_1 in the neutral atmosphere with $n = n_1$ to a different neutral atmosphere $n = n_2$ as follows:

$$F_2(h_2) = F_1(h_1) = F_1(Ah_2 + B). \tag{5}$$

The constant B represents a vertical shift of the profile F_1 and the constant A modifies the shape of profile F_1. If $H_2 > H_1$ ($H_2 < H_1$) and $n_{02} = n_{01}$, the profile F_2 will be at higher (lower) altitudes than the profile F_1 with gradients of F being increased (decreased). If instead $H_2 = H_1 = H$ then Eq. (4a) gets the form

$$h_2 = h_1 + H \ln(n_{02}/n_{01}) \tag{6}$$

implying that the vertical shift of the profile F and, say, the height of its maximum value, are quite insensitive to the variations in n_0.

The modification of F can be analyzed quantitatively by studying how much the curve in Fig. 12 is deformed from $H_1 = 6.3$ km to $H_2 = 3.4$ km. Furthermore, let us analyze the case $n_2(h = 120 \text{ km})/n_1(h = 120 \text{ km})(= [n_{02} \exp(-120 \text{ km}/H_2)]/[n_{01} \exp(-120 \text{ km}/H_1)]) = 100$ that is unrealistically high density increase at Mars but which is useful to illustrate the deformation of the profile F and the insensitivity of the horizontal shift to the density. As seen in Fig. 12, reducing the neutral scale height results in increased gradients and it produces a sharp peak. The peak value is moved only about 10 km higher because even a large change in n_{02}/n_{01} changes only little the constant B in Eq. (4b).

The properties of the martian atmosphere have received much more attention than the properties of martian H-ENAs and it is therefore instructive to consider the question how the profiles associated with impacting particles, for example, as shown in Fig. 12, are related with the martian ionosphere. Equations (4a) and (4b) can be used to calculate how the altitude of a certain point in the profile F changes when the density changes, for example, the altitude h_{max} when F is in its maximum. As seen in Eqs. (4a) and (4b), higher neutral densities (by increasing H or n_0) result in a higher h_{max}. The maximum value varies therefore in concert with the altitude of the maximum production rate, z_{peak}. In the idealized Chapman model (see, e.g., Chamberlain and Hunten, 1987, p. 230)

$$z_{peak} = z_0 + H \ln\big(\sigma_{hf} n_0 H / \cos(\text{SZA})\big). \tag{7}$$

Here σ_{hf} is the phoionization cross section and n_0 is the neutral density at the height z. The Chapman production function does not depend purely on the column density N and, therefore, it cannot be scaled from one density profile to another according to Eqs. (4a) and (4b) as in the CSDA model. Furthermore,

the functional form of the Chapman production function is not identical with the energy deposition or the ionization profiles associated with impacting particles in a 3-D MC model or in CSDA approximation. Differences between the effects associated with the precipitating particles and the effects associated with impacting photons result from the fact that impacting particles interact with many atmospheric neutrals. The atmospheric effects are therefore spatially spread within the volume inside which the particle makes a zig-zag motion, its energy decaying to smaller energies. In the ideal Chapman layer model, instead, the absorption of a photon, whose path is a straight line, takes place in one point. It is interesting to note that despite of these obvious differences between the impacting particles and photons some similarities, at least in terms of mathematical formalism, can be found between the processes. For example, the peak of the Chapman production function [Eq. (6)] is one of the three terms that gives the peak ionization altitude in 3-D MC model (see Kallio and Barabash, 2001, for details).

7.2. Magnetized upper atmosphere

The non-scattered H-ENAs can spend part of their time in the atmosphere as H^+ and being under the influence of the Lorentz force. This is particularly important factor on the Southern hemisphere which is magnetized due to the martian crustal anomalies. Another source of the magnetic field in the upper atmosphere can be associated with the interaction between the solar wind plasma and the martian atmosphere. The so-called induced magnetic field produces a magnetic field above the Northern hemisphere and modifies the initial crustal magnetic field above the Southern hemisphere. A quantitative analysis of the effects of the magnetic and electric fields to the properties of the scattered H-ENAs would require a fine resolution self-consistent model 3-D model. Such a comprehensive study remains to be done in the future and here only some possible quantitative effects are discussed.

The magnetic field constrains the charged particle motion perpendicular to the field lines. One may therefore expect that a strong magnetic field tangential to the surface may reduce the motion of H^+ ions toward Mars and, consequently, increase the scattering altitude compared with the non-magnetized upper atmosphere case. A tangential magnetic field is therefore anticipated to shift the minimum altitude profiles in Fig. 12 to higher altitudes

The radial magnetic field component, in contrast, is also expected to affect the properties of scattered H-ENAs. First, the gyromotion can quickly, in about half a gyroperiod, change the direction of the H^+ from downward moving to upward moving ion. The information about the original velocity of the particle (downward) can therefore quickly be lost. The path of a gyrating ion also exceeds the length of the ion compared with the length of which its guiding center moves and, therefore, H^+ are expected to move horizontally and vertically smaller distances than they would without the magnetic field. A magnetic cusp like structure, instead, can cause focusing of the H^+ and affect the intensity of the scattered H-ENAs.

In a rigorous study the effects of the magnetic and electric fields to the H-ENA scattering should be studied by a numerical 3-D MC model. Nevertheless, it is worth noting that, at least in principle, differences between a non-magnetized and magnetized scattering case include information about the magnetization stage of the upper atmosphere, both in terms of the absolute magnetic field and the direction of the magnetic field. The scattered H-ENAs may therefore carry direct information about the plasma properties of the upper atmosphere.

8. Discussion and summary

The main goal of this paper was to study the properties of hydrogen atoms produced upstream of the bow shock. That analysis was performed by using a 3-D MC model (Sections 2–6). The solar wind H-ENAs are imbedded in H-ENAs produced downstream of the bow shock and therefore the possibility to distinguish these two populations is an issue, especially from the measurement point of view. To that aim the total fluxes of H-ENAs were derived separately in the downstream and upstream of the bow shock in the LoS integration by using an empirical plasma model (Section 6). Finally, the altitude range from which the scattered H-ENAs arrive was discussed in Section 7.

Charge exchange processes are not restricted on Mars because they can take a place whenever plasma interacts with neutrals. It is therefore important to consider what the results presented in this paper can tell about (1) different H-ENA populations near Mars, and about (2) the neutral atmosphere which scatters H-ENAs.

8.1. ENAs formed upstream vs downstream of the bow shock

In the paper, the scattered solar wind H-ENAs produced back-scattered H-ENA flux, that within the limb of Mars can exceed the H-ENA flux produced downstream of the bow shock when viewed on the dayside (Fig. 10). On the nightside the scattered solar wind H-ENAs form a limb brightening (Fig. 4) corresponding a maximum flux of order of $\sim 1 \times 10^6$ cm^{-2} s^{-1} str^{-1} on the nightside at $x \sim 1.8 R_M$ (Fig. 7). The limb brightening takes a place near Mars within an ENA thick region from which the flux of H-ENAs would have been decreased ("limb dimming") without scattered H-ENAs. Whether the limb brightening due to the scattered H-ENAs produces a flux that exceeds the flux of H-ENAs slightly away from the limb depends on how intensively H-ENAs are produced in the magnetosphere and in the magnetosheath.

The estimation of H-ENA production near Mars at altitudes less than a few hundred kilometers above the surface is highly uncertain because the properties of H$^+$ ions at those altitudes are unknown. However, an estimation based on LoS suggests that the limb brightening may be imbedded in the nearby H-ENA flux with about the same total maximum flux ($\sim 1 \times 10^6$ cm^{-2} s^{-1} str^{-1}) as the flux from the limb (cf. Figs. 7b or 7d with Fig. 11c). An ENA instrument without energy resolution may therefore have difficulties in distinguishing the scattered solar wind H-ENAs from the H-ENAs produced down-

stream of the bow shock unless the FOV of the instrument is small enough to resolve the limb region at $100 < h < 200$ from the region just above it. The velocity distribution of the scattered solar wind H-ENAs carries information about the velocity distribution of the initial solar wind H-ENAs (see Kallio and Barabash, 2001, Fig. 5) and, therefore, an ENA instrument with energy resolution may help to distinguish the scattered solar wind H-ENAs from the other H-ENA population. Whether H-ENA fluxes associated with the upstream and downstream ENAs can in practice be distinguished in the energy spectra requires a self-consistent 3-D Mars–solar wind interaction model and is therefore far beyond the scope of the present study.

8.2. ENA sounding technique and the properties of the scattering atmosphere

The intensity of the scattered H-ENAs from a given LoS direction depends on the atmospheric neutral profile and the properties of the plasma. The measured H-ENA fluxes provide therefore a possibility to invert the properties of the plasma and the density of the atmosphere. Whether such an ENA inversion is possible in practice, depends on the spatial and energy resolution of an ENA instrument. A poor energy resolution precludes distinguishing the scattered population from the non-scattered population. A poor spatial resolution makes it impossible to study how the intensity varies with altitude from the surface.

The altitude of the scattering depends on the neutral density profile as is the case also for the altitude of the ionosphere peak density. The peak of the ionosphere has been found to vary with the activity of the Sun (Mendillo et al., 2003; Martinis et al., 2003) and to depend on the topographic changes below the ionosphere (Wang and Nielsen, 2004), and exhibits, for example, longitudinal variations (Bougher et al., 2004) that modify the density of the upper atmosphere. These density changes are also anticipated to affect the altitudes where the scattering takes place (cf. Section 7.1) and, consequently, the spatial H-ENA emission intensity from Mars. Magnetization of the upper atmosphere is also expected to affect the scattering altitude and, therefore, the measured H-ENA intensities (cf. Section 7.2).

The ENA sounding technique is anticipated to provide a tool to study the densities and magnetization of the upper atmospheres at the other Solar System bodies than Mars. Venus does not have a notable intrinsic magnetic field but it has a dense atmosphere. The dominant atmospheric neutral species at Venus is CO_2 as in the martian atmosphere. The properties of H-ENAs presented in this paper can therefore be expected also to illustrate the properties of scattered H-ENAs at Venus due to similar major collision processes. A comprehensive scattering study of H-ENAs at Venus should be based on a 3-D MC model that includes venusian atmosphere profiles that cannot be described purely with the SZA and the height. However, some insight into the Venus case may be obtained by mapping the profiles that describe the effect of the precipitating particles at Mars (e.g., ionization, energy deposi-

tion, photoemission) as well as the scattering minimum altitude profile given in Fig. 12. If we approximate the neutral temperature at Venus in the altitude range ~ 80 km $< h < 140$ km to be $T_2 = 170$ K (see Chamberlain and Hunten, 1987, p. 27, for the measured temperature profiles below 200 km) and the neutral temperature at Mars at the same altitude range $T_1 = 130$ K (for the measured temperature profiles below 200 km see Chamberlain and Hunten, 1987, p. 44, and references therein). These temperatures correspond to the neutral scale heights for CO_2 of $H_{Mars} = H_1 = 6.3$ km and $H_{Venus} = H_2 = 3.4$ km. Furthermore, the density at Venus at $h = 120$ km is about 100 times larger than the density at Mars at $h = 120$ km, that is, $n_{Venus}(h = 120$ km$)/n_{Mars}(h = 120$ km$) = 100$. These scale height and density ratios are the same as in Fig. 12 to illustrate how the minimum altitude function resulting from a 3-D MC is transformed when the atmosphere profile is changes according to Eqs. (4a) and (4b). The shift of the original minimum altitude profile upward about 10 km illustrates therefore how the scattering altitude profile changes from the martian atmosphere density profile to the venusian altitude profile according to Eqs. (4a) and (4b). The applicability of Eqs. (4a) and (4b) to describe various atmospheres relays naturally on how accurately the CSDA model describes the analyzed atmospheric region. Especially, a height-dependent T, that is the case, for example, in the Earths thermosphere above 100 km, or changes of the dominant ion species with altitude, lead to scattering problems that needs to be solved by 3D MC model.

The Moon provides an example of an object without an atmosphere. At the Moon the magnetic field prevents rapid filling of the Lunar tail with ions (see, e.g., Kallio, 2005). The hydrogen ENAs formed in the Earth's hydrogen exosphere can, however, fill the Lunar wake in a similar way as the non-scattered solar wind ENAs fill the martian tail region. Measurements of ENAs in the Lunar wake can therefore be used to monitor the properties of the solar wind plasma, or the Earth's magnetosheath plasma, and, consequently, some of the key parameters for the understanding of how plasmas interact with the Moon. Martian moon Phobos provides also a non-atmospheric object which is a target of H-ENAs (formed in the martian hydrogen exosphere). The Moon and Phobos can be regarded as objects with zero neutral scale heights because H-ENAs interact directly with the upper layers of their surfaces. In these cases H-ENAs within their optical shadow are mainly non-scattered solar wind ENAs.

Active comets, on the other hand, provide another type of objects that have a spatially extended (up to millions of kilometers) dense neutral particle environment while the radius of the nucleus itself can be very small, on the order of kilometers. The H-ENAs near the nucleus are scattered H-ENAs. Mars and Venus can be regarded as intermediate cases between these two extreme cases of Lunar and cometary H-ENA interaction.

References

Acuña, M.H., and 19 colleagues, 1998. Magnetic field and plasma observations at Mars: Initial results of the Mars Global Surveyor mission. Science 279, 1676–1680.

Barabash, S., and 46 colleagues, 2004. The Analyser of Space Plasmas and Energetic Atoms (ASPERA-3) for the European Mars Express Mission. ESA Publ., SP-1240. ESA, Noordwijk, pp. 121–139.

Bougher, S.W., Engel, S., Hinson, D.P., Murphy, J.R., 2004. MGS radio science electron density profiles: Interannual variability and implications for the martian neutral atmosphere. J. Geophys. Res. 109, doi:10.1029/2003JE002154.

Brinkfeldt, K., and 46 colleagues, 2006. First ENA observations at Mars: Solar-wind ENAs on the nightside. Icarus 182, 439–447.

Chamberlain, C.W., Hunten, D.M., 1987. Theory of Planetary Atmospheres: An Introduction to Their Physics and Chemistry. In: International Geophysics Series, second ed., vol. 36. Academic Press, San Diego, CA.

Futaana, Y., and 46 colleagues, 2006. First ENA observations at Mars: ENA emissions from the martian upper atmosphere. Icarus 182, 424–430.

Gunell, H., Holmström, M., Barabash, S., Kallio, E., Janhunen, P., Nagy, A.F., Ma, Y., 2005. Planetary ENA imaging: Effects of different interaction models for Mars. Planet. Space Sci., doi:10.1016/j.pss.2005.04.002.

Gunell, H., and 46 colleagues, 2006. First ENA observations at Mars: Charge exchange ENAs produced in the magnetosheath. Icarus 182, 431–438.

Holmström, M., Barabash, S., Kallio, E., 2002. Energetic neutral atoms at Mars. I. Imaging of solar wind protons. J. Geophys. Res. 107 (A10), doi:10.1029/2002JA000325. 1277.

Kallio, E., 2005. Formation of the lunar wake in quasi-neutral hybrid model. Geophys. Res. Lett. 32, doi:10.1029/2004GL021989. L06107.

Kallio, E., Barabash, S., 2000. On the elastic and inelastic collisions between the precipitating energetic hydrogen atoms and the martian atmospheric neutrals. J. Geophys. Res. 105. 24973.

Kallio, E., Barabash, S., 2001. Atmospheric effects of precipitating energetic hydrogen atoms on the martian atmosphere. J. Geophys. Res. 106, 165–178.

Kallio, E., Janhunen, P., 2001. Atmospheric effects of proton precipitation in the martian atmosphere and its connection to the Mars–solar wind interaction. J. Geophys. Res. 106, 5617–5634.

Kallio, E., Luhmann, J.G., Barabash, S., 1997. Charge exchange near Mars: The solar wind absorption and neutral atom production. J. Geophys. Res. 102, 22183–22197.

Kallio, E., and 46 colleagues, 2006. Ion escape at Mars: Comparison of a 3-D hybrid simulation with Mars Express IMA/ASPERA-3 measurements. Icarus 182, 350–359.

Martinis, C.R., Wilson, J.K., Mendillo, M.J., 2003. Modelling day-to-day ionospheric variability on Mars. Geophys. Res. Lett. 108, doi:10.1029/2003JA009973.

Mendillo, M., Smith, S., Wroten, J., Rishbeth, H., Hinson, D., 2003. Simultaneous ionospheric variability on Earth and Mars. J. Geophys. Res. 108, doi:10.1029/2003JA009961.

Wang, J.-S., Nielsen, E., 2004. Evidence for topographical effects on the martian ionosphere. Planet. Space Sci. 52, 881–886.